Materials & Design 253 (2025) 113823

Contents lists available at ScienceDirect

Materials & Design

journal homepage: www.elsevier.com/locate/matdes

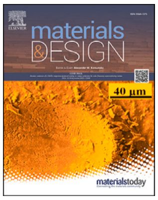

Thermophysical and microstructural characterization of Ti-6Al-4V in powder and laser powder bed fusion-processed state within the global temperature field range

J. Rottler [a,*], T.K. Tetzlaff [b], A. Wohninsland [b], A. Lion [a], M. Johlitz [a]

[a] Institute of Mechanics, University of the Bundeswehr Munich, Werner-Heisenberg-Weg 39, Neubiberg, 85579, Germany
[b] Bundeswehr Research Institute for Materials, Fuels and Lubricants (WIWeB), Institutsweg 1, 85435, Erding, Germany

ARTICLE INFO

Keywords:
Ti-6Al-4V
Thermal analysis
Microstructure
Laser powder bed fusion
Powder
Thermal conductivity

ABSTRACT

To pave the way for thermophysical modeling and further PBF-LB/M process optimization, the thermophysical properties of Ti-6Al-4V in powder and processed states were investigated using thermo-mechanical analysis, laser flash analysis, and differential scanning calorimetry. Microstructural characterization using SEM, Vickers hardness testing, and XRD facilitated a novel interpretation of the results. The macroscopic density exhibited a linear relationship up to 880 °C, showing only a minor impact from microstructural effects. The evolution of α' martensitic microstructure was analyzed by examining linear thermal expansion coefficients indicating direction dependency. During heating, the precipitation and stabilization of β provoke the formation and decomposition of the intermetallic phase, accompanied by a significant increase in hardness and an exothermic event. Additionally, the relaxation of residual stresses and transformation into the β phase determines the microstructural evolution. Thermal diffusivity of as-built Ti-6Al-4V propagates linearly up to 950 °C. For powder, HotDisk measurements corroborate laser flash data obtained up to 850 °C. Based on the LFA, the start of sintering is identified and attributed to a change in the heat transfer mechanism in AM powders. Specific heat capacity and effective thermal conductivity of AM Ti-6Al-4V are determined, highlighting the shortcomings of predicting AM powders' conductivity based on solid materials.

1. Introduction

In additive manufacturing (AM), the Laser Powder Bed Fusion (PBF-LB/M) is a fabrication method in which components are manufactured by selective laser scanning of a metal powder. Adding powder layer by layer and repeating the selective scanning procedure generates a solid three-dimensional component from the powder material embedded in the non-solidified powder bed. The absence of component-specific equipment requirements and the ability to manufacture complex geometries make PBF-LB/M particularly attractive for aerospace, medical technology, and motorsports applications. These applications impose high demands on the used materials, with the high-strength and low-weight titanium alloy Ti-6Al-4V being a material of choice. To further develop the capability and tailor the PBF-LB/M method with Ti-6Al-4V, gaining knowledge about the process physics and the material behavior is the focus of ongoing research. In particular, the flow of process heat from the laser-scanned layer surface is critical, as inadequate heat removal is associated with defects such as warping [1–3] and compromised component quality [4–8].

In behalf of the laser's focused and dynamic energy input, the material undergoes a unique order of transformations from the powder state to the liquid state and several solid-state phase transformations. For Ti-6Al-4V, the temperature history within the PBF-LB/M process provokes a characteristic microstructure. The heat impact is classified into the temperature field's local and global range of influence [9–12]. Within the local range of influence, the material is molten, rapidly solidified, and re-melted due to the bypassing laser focus spot. In this range, melt pool physics with temperatures up to 4000 K, cooling gradients up to 5-20 $\frac{\mathrm{K}}{\mu\mathrm{m}}$, and cooling rates up to 1-40 $\frac{\mathrm{K}}{\mu\mathrm{s}}$ are the driving mechanisms [8,12]. After melting, the liquid phase rapidly solidifies into the body-centered cubic (bcc) β phase, transforming into a martensitic structure during further rapid cooling. In PBF-LB/M-processed Ti-6Al-

---

* Corresponding author.
E-mail address: johannes.rottler@unibw.de (J. Rottler).
URL: https://www.unibw.de/lrt4 (J. Rottler).

https://doi.org/10.1016/j.matdes.2025.113823
Received 20 December 2024; Received in revised form 3 March 2025; Accepted 7 March 2025

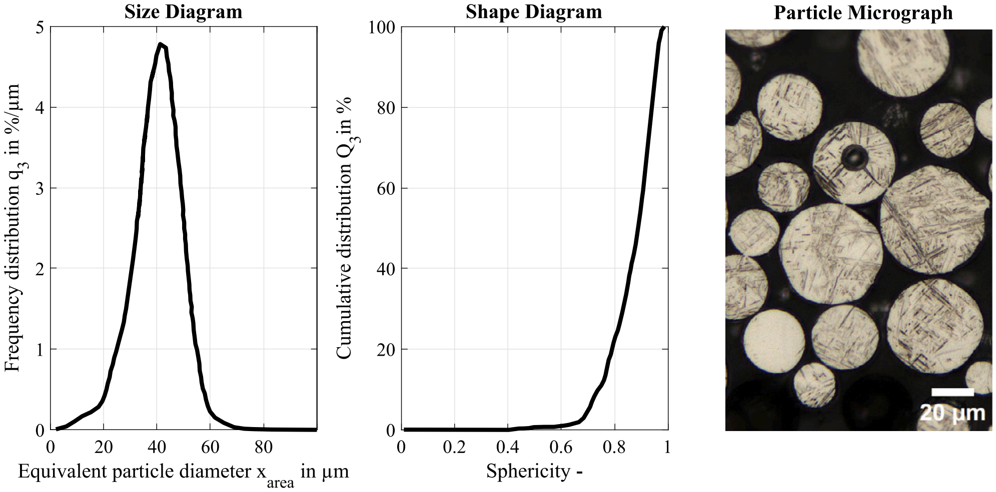

Fig. 1. Size and shape distribution of pristine Ti-6Al-4V powder and micrograph of powder particles under an optical microscope indicating martensitic microstructure.

4V, this structure typically appears as a lamellar and acicular configuration within the former β grain boundaries, exhibiting a hexagonal close-packed (hcp) crystal structure known as α'-martensite, though a diffusionless, shear-like mechanism [13]. Due to the track-wise and layerwise nature of the process, this leads to a characteristic columnar microstructure observable in micrographs [3,14]. The global heat affected zone is characterized by several cooling and reheating cycles where temperatures remain below the melting range. However, the solid-solid phase transformations highly depend on the maximum temperature and the cooling rate. If the β-transus temperature is reached, which is observed at around 1000 °C [15,16,3,17,18,12], a lamellar and acicular α' martensitic microstructure is formed [13,16,12]. The ongoing periodic heating with decreasing temperature peaks provokes the evolution of hierarchical martensitic structure. It consists of primary, secondary, tertiary, and quaternary α' martensite [10,14]. In comparison, conventionally hot-rolled or usually post AM process heat-treated Ti-6Al-4V exhibits an $\alpha+\beta$ microstructure [19,3,17,12]. Differences in microstructure result in anisotropic properties, including increased yield and tensile strength, reduced ductility in the build-up direction [3,10,17], and enhanced corrosion resistance [20,21]. These property variations are closely linked to process parameters and scanning strategies, which influence the martensitic microstructure through the thermal history [22,14]. Furthermore, some investigations observe a more complex microstructure with partial α and remaining β besides mainly acicular α' martensite [22,21]. This underlines the necessity for future research endeavors to attain a thorough and comprehensive understanding of heat flow and its effect on the process. As the material in the PBF-LB/M process experiences a transition from the initial powder via highly dynamic melting to a solid state, these two states govern the heat flow behavior. In the solid state, the heat is transferred by conduction and determined by the associated thermophysical properties. To investigate the β-transus temperature of PBF-LB/M-processed Ti-6Al-4V in the processed state, Liang et al. [15] and Bartsch et al. [23] used scanning calorimetry. Bartsch et al. [23] also reviewed existing literature on thermophysical properties and contributed new data through laser flash analysis, highlighting a current lack of detailed experimental data, especially for AM powders [23]. In powder beds under inert gas atmosphere, the heat is transferred by several mechanisms, like conduction through the particle material itself, heat transfer through the contact areas between particles, conduction in the gas, and radiation between solid surfaces. Under a continuum-mechanical approach, these mechanisms are considered to be lumped and referred to as effective thermal conductivity [24–27]. However, experimental studies on the thermophysical properties of AM powders remain sparse [23,28,29,24,25]. Ahsan et al. [29] and Liu et al. [24] examined selected powder materials, including Ti-6Al-4V, via laser flash and, respectively, transient plane method and compared their results to analytical models. Both studies concluded that known analytical models for powders used in AM cannot predict temperature-dependent properties due to the changing mechanisms of heat transfer with rising temperature. By testing Ti-6Al-4V with different particle size distributions under argon up to 750 °C, Lui et al. [24] found that below 300 °C, gas-gas and gas-solid conduction dominate heat transfer, while above 400 °C, particle agglomeration and material-dependent effects play a significant role, enhancing effective thermal conductivity. Wei et al. [28] used the transient hot wire method for measuring the effective thermal conductivity of Ti-6Al-4V material powders under argon, nitrogen, and helium atmospheres and pressure levels and stated increasing values with rising temperatures up to 200 °C. Zhang et al. [25] employed a laser flash analysis supported approach to calculate the effective thermal conductivity from printed samples with enclosed loose powder. Via finite element simulation and a multivariate inverse method, a linear trend is observed between 100 °C and 500 °C. Although promising, these approaches are labor-intensive and prone to interference.

All in all, gaining a deeper understanding of transient and inhomogeneous temperature fields is necessary to design a reliable process that delivers adequate component quality, which is a current engineering challenge. While fundamental knowledge of materials process behavior and macro-scale process simulation is powerful, the literature indicates a lack of significant expertise in this area. Consequently, this study focuses on examining the thermophysical properties of Ti-6Al-4V within the global temperature distribution occurring in the PBF-LB/M process. Samples of pristine powder in its unused state (powder) and PBF-LB/M processed solid state (as-built) are experimentally analyzed using calorimetric, thermo-mechanical, and transient thermal methods alongside fundamental material characterization techniques. This enables new results from a macroscopic point of view to be obtained on the thermal expansion behavior, the thermal diffusivity, and the thermal conductivity, in dependence on the process temperature. Investigations on the process-specific microstructure should allow a detailed discussion of the complex trends of thermophysical properties. Additionally, the capabilities and limitations of thermal analysis methods are critically assessed.

2. Methodology

2.1. Powder samples

As feedstock material one batch of pre-alloyed and gas atomized Ti-6Al-4V with extra low interstitials quality (Grade 23) supplied by EOS GmbH Electro Optical Systems was used. The samples for powder analysis were taken from the one batch in pristine condition with a core multi sampler (Bürkle GmbH, Germany). The particle size and shape distribution (see Fig. 1) was analyzed via dynamic image analysis with

Table 1
Chemical composition of unused Ti-6Al-4V ELI powder and as-built sample.

Sample	Element	Al	V	O	N	H	Fe*	C*	Ti
powder	wt.%	6.23	3.76	0.119	0.035	0.004	max. 0.25	max. 0.08	bal.
as-built	wt.%	6.51	3.95	0.145	0.022	0.008	max. 0.25	max. 0.08	bal.

* value from data sheet, not measured [32].

a CAMSIZER X2 by Microtrac RETSCH GmbH according to ISO 13322-2 [30]. The powder particles measure an equivalent particle diameter of 25.4 µm (D_{10}), 37.6 µm (D_{50} - Median) and 46.4 µm (D_{90}) and a mean value of 36.8 µm. The shape distribution is characterized by the arithmetic-mean value of sphericity of 0.88 (with reference to DIN EN ISO 9276-6 [31]). The present results provide evidence of the powder's quality, characterized by sharp and normally distributed particle size and a precise and uniform spherical shape. Table 1 shows the chemical composition of the powder batch which was analyzed on a sample using optical emission spectrometry with inductively coupled plasma, and IR-spectrometry after melt extraction. The density of the particles (skeletal density) was measured with a helium pycnometer by Anton Paar of the type Ultrapyc 5000 to 4.4140 $\frac{\text{g}}{\text{cm}^3}$.

2.2. As-built samples

The as-built samples were fabricated using a TruPrint1000 Multilaser by Trumpf SE + Co. KG. This PBF-LB/M system operates with two fiber laser and f-theta lenses optics, providing two continuous scanning lasers at a wavelength of 1070 nm. The laser focus spot diameter is 55 µm. The process is shielded under an argon atmosphere with an oxygen ratio below 0.01%. The scanning parameters are set to 110 W laser power, 905 $\frac{\text{mm}}{\text{s}}$ scan speed, and an 80 µm hatching distance with a parallel line scan pattern and rotating pattern angle of 67° in layers of 20 µm powder height. The density of 4.4175 $\frac{\text{g}}{\text{cm}^3}$ of the printed sample components was measured using the helium pycnometer which leads to a porosity of ≈0.6%. The samples for thermal analysis were taken from one print job and cut with a diamond wire saw supplied by WELL DWS SA to prevent heat input during sample preparation.

2.3. Thermo mechanical analysis TMA

The thermal expansion behavior was investigated using thermo mechanical analysis (TMA) via a TMA 402 F1 Hyperion supplied by NETZSCH. The device is equipped with a type K sensor and argon 5.0 is used as purge gas. During the measurement the samples were heated from 25 °C up to 900 °C with a heating rate of 10 $\frac{\text{K}}{\text{min}}$ under a static force of 1 N. The method was calibrated with an aluminum oxide standard. The as-built samples had a quadratic cross-section with 5 mm x 5 mm and a total height of 20 mm. The exact dimensions of all samples were measured using a micrometer screw with a precision of ±10 µm, and these measurements were used to calculate the coefficient of thermal expansion. With the utilized scanning strategy, which includes layerwise 67° rotation of the scan pattern angle, homogeneous microstructure in the in-layer direction is intended [33,34]. Therefore, the as-built samples were fabricated and tested transversally and along the build-up direction. For powder evaluation the powder sample was placed in an aluminum oxide cylindrical sample holder with an inner sample volume of Ø5.5 mm x 6 mm and a piston as lid.

2.4. Laser flash analysis LFA

The laser flash analysis (LFA) is one of the transient methods in thermal analysis to determine the thermal diffusivity. In this work a LFA 467 HT by NETSCH was used. With this device, one side of a sample is flashed with a xenon light while the temperature on the counter side is logged by an IR-detector. Analytical models are fitted to each flash's time-temperature behavior in the evaluation software. The sample's thermal diffusivity is calculated based on the assumptions of the heat transfer model and the sample height. Comparable to the other analysis methods argon 5.0 was used as purge gas. For as-built samples disks were cut from fabricated cylinders with a diameter of Ø11.98 mm and a height of 2.92 mm by described the diamond wire saw. The sample surfaces were sandblasted to increase the absorption of the xenon light flash. Three measurements were driven at each temperature step ranging in from 25 °C until 950 °C. The powder samples were prepared in a transparent sapphire sample holder with the inner dimensions of Ø10.97 mm x 1.977 mm. Four series of measurements were carried out whereas the holder was packed with powder and leveled twice with a spatula to achieve a smooth powder surface. With this procedure 504.993 mg for the first, 508.008 mg for the second, 509.547 mg for the third, and 498.570 mg for the fourth run of powder was tested resulting in a powder apparent density of 2.70±0.04 $\frac{\text{g}}{\text{cm}^3}$. In each run multiple flashes were measured between 30 °C and 850 °C.

2.5. Transient plane source method HotDisk®

As a further representative of transient thermal analyses the transient plane source method (HotDisk® method) was used to estimate and validate the thermal diffusivity measurements. The HotDisk® sensor operates both as heat source and as dynamic temperature sensor. The sensor is inserted centrally into the sample. With a defined electrical heating power (in W) and a measurement duration (in s), a specific amount of energy is applied to the center of the samples by the sensor and the temperature change of the sample is measured over time. The experiments were carried out with a TPS 2500s system supplied by Hot-Disk® and equipped with the kapton sensor Ø6.378 mm and coverage. To measure at room temperature, 30 °C, 50 °C, and 100 °C, the setup was placed in a laboratory furnace. Sufficient heating times and time intervals between data recording were considered. The as-built samples were cut from a cylinder with the diameter of Ø19.90 mm and with a height of 5.02 mm. For powder evaluation, a tube with an inner diameter of Ø19.9 mm was filled with 8 mm of powder, the sensor was inserted through a cut in the tube wall on the plane powder surface, and the tube further filled with 7 mm. A total of 12.925 g of powder was filled in, resulting in an estimated apparent density of 2.8±0.1 $\frac{\text{g}}{\text{cm}^3}$.

2.6. Differential scanning calorimetry DSC

Differential scanning calorimetry (DSC) was utilized to investigate the phase characteristics within the temperatures observed globally during the PBF-LB/M process. To carry out this experiment, a heat-flux type STA 449 F1 Jupiter by NETZSCH was equipped with a type S sensor and argon 5.0 as purge gas. A platinum-rhodium crucible with aluminum oxide liner and a pierced lid was used. For the DSC measurement and the evaluation of the specific heat capacity according to the ratio method, an isothermal phase with 30 °C is followed by a constant heating phase up to 1100 °C. Referring to DIN 51007 a heating rate of 20 $\frac{\text{K}}{\text{min}}$ is ensured. The measurement procedure was calibrated with indium, aluminum, and zinc. Measurements with empty crucibles with pierced lids were carried out as references and for baseline correction. A sapphire standard of 49.9 mg was measured for specific heat capacity calculation. The as-built samples with a comparable mass were prepared as described. Furthermore, the bottom surfaces of the samples were wet-sanded and cleaned with isopropanol before weighing to ensure an adequate and

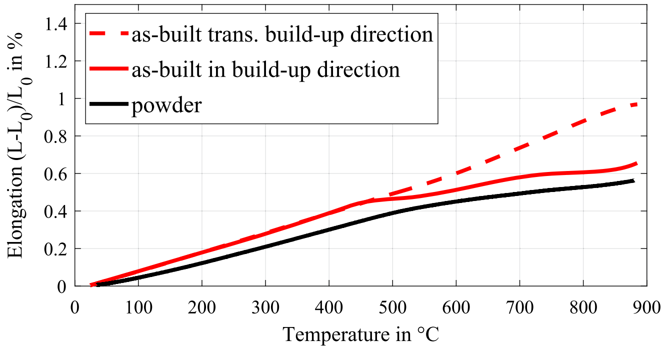

Fig. 2. Thermal elongation of as-built sample tested in build-up direction and transversal to build-up direction and powder Ti-6Al-4V samples during heating with 10 $\frac{\mathrm{K}}{\mathrm{min}}$.

fully-faced contact with the crucible, which proved crucial for successful data collection.

2.7. Metallurgical characterization

In order to analyze the microstructural transformation mechanisms, as-built samples of the dimension 10 mm x 10 mm x 10 mm were manufactured, heat-treated in a laboratory furnace under an air atmosphere at selected holding temperatures for 30 minutes, followed by quenching in water. For scanning electron microscopy (SEM), heat-treated samples were sectioned using a diamond wire saw at the center of each sample. The mid surface was then ion polished with the HITACHI Ion Milling System ArBlade5000. During the polishing process, the temperature of the cross-section milling stage was kept at 0 °C to prevent any changes in the microstructure. Subsequently, SEM was conducted using a ZEISS Ultra Plus equipped with an In-lens detector operating in SE2 mode (1 kV) and a 60 μm shutter.

The Vickers hardness was investigated on sectioned samples embedded in epoxy resin. The sample surface was grinded with SiC paper until a grit size of 400 and polished with MD-Mol 6 μm and polishing suspension. Hardness HV5 was measured using the Qness Q10A+ universal hardness device by ATM Qness GmbH with a static measurement force of 49.03 N over 10 seconds. A minimum of 9 idents were measured in the center of each sample.

The X-ray diffraction (XRD) analysis was performed using a BRUCKER D8 Discover with a Cu-Kα tube set to 40 kV and 40 mA in line focus. An optical Ni filter with a 2.5° axial Soller and an 8 mm detector shutter was utilized, along with a LynexEye XE detector. Scanning was conducted with a step size of 0.02° and a collection time of 2 seconds per step. The quantitative Rietveld phase fraction analysis was carried out using the TOPAS V6 software package.

3. Results and discussion

3.1. Thermal elongation behavior and density

Fig. 2 shows the macroscopic thermal elongation curves of the as-built and powder samples measured by TMA. For additional detail, the differential coefficient of thermal expansion is provided in Fig. 5. At the starting temperatures, the powder samples exhibit a delayed increase in elongation compared to the as-built samples. This is attributed to a densification of the powder in the sample holder by a compaction of the powder particles. Subsequently, the thermal elongation of all samples continues almost linearly. In the as-built samples, the elongation trend in the transverse-to-build-up direction remains linear across the examined temperature range. In contrast, the as-built samples measured in the build-up direction and the powder samples exhibit slope changes in slope at 458.6 °C (onset temperature for the as-built in the build-up direction) and 548.3 °C (onset temperature for the powder). These differences can be attributed to the highly oriented microstructure, particularly grain boundaries aligned in the build-up direction, which predominantly influence macroscopic elongation in the transverse direction. However, the microstructural transformation mechanisms dominate the macroscopic elongation behavior in the build-up direction. The powder particles and the as-built samples contain martensitic α', formed due to rapid cooling during their respective fabrication processes. However, the temperature history in additive manufacturing, involving multiple heating cycles, results in a hierarchical microstructure [10]. This contrasts with the non-periodic cooling temperature history of the gas-atomization process and could be an explanation for different onset temperatures and trends.

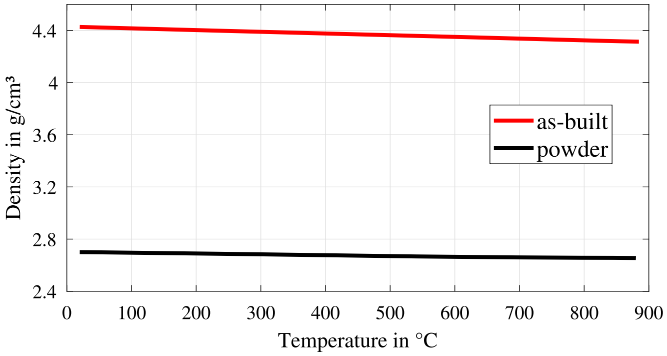

Fig. 3. Calculated density progression for powder (isotropic expansion) and as-built state (transversal isotropic expansion behavior).

The experimental data of the elongation behavior enables the evaluation of the macroscopic temperature-dependent density of the AM Ti-6Al-4V in both the powder and the as-built state. With the assumption of isotropic expansion behavior, the powder density ρ_p evolution is calculated, with the powder apparent density at room temperature ρ_p0, and the thermal expansion ϵ_xyz, by [35]:

$$\rho_p(\theta) = \rho_{p0} \cdot \frac{1}{(1+\epsilon_{xyz}(\theta))^3}; \tag{1}$$

The density of the as-built state ρ_ab is determined by hypothesizing transversal isotropic expansion behavior, characterized by ϵ_z in build-up direction and thermal expansion ϵ_xy transversal to build-up direction. Accordingly, the density is calculated based on the density of the fabricated samples at room temperature ρ_ab0 as [35]:

$$\rho_{ab}(\theta) = \rho_{ab0} \cdot \frac{1}{(1+\epsilon_{xy}(\theta))^2 \cdot (1+\epsilon_z(\theta))}; \tag{2}$$

The results for the calculated density progressions from room temperature to approx. 880 °C are represented in Fig. 3. The density in the as-built state decreases from 4.4175 $\frac{\mathrm{g}}{\mathrm{cm}^3}$ to 4.314 $\frac{\mathrm{g}}{\mathrm{cm}^3}$ and the apparent powder bed density from 2.70 $\frac{\mathrm{g}}{\mathrm{cm}^3}$ to 2.65 $\frac{\mathrm{g}}{\mathrm{cm}^3}$. Consequently, the influence of changes in the microstructure with the global temperature range on the macroscopic density evolution is rather small within the almost linear progression.

3.2. Microstructure and phase transformation

The established DSC method is known for quantitatively measuring heat effects (enthalpies) and their associated temperatures. Thus, it allows conclusions to be drawn about the physical and chemical transformation mechanisms in the microstructural state. Fig. 4 represents the obtained DSC data from the AM samples during heating. The powder and as-built samples exhibit two peaks within the examined temperature range. For the powder sample, the first peak is characterized by an extrapolated initial temperature θ_ei1 of 431.3 °C and an extrapolated finish temperature θ_ef1 of 603.4 °C. Similarly, for the as-built sample, the first peak is defined by an extrapolated initial temperature θ_ei1 of

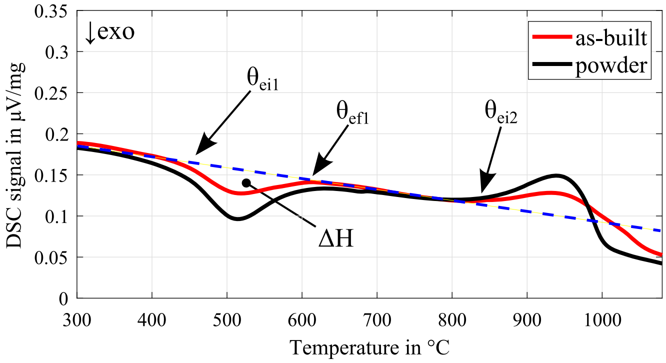

Fig. 4. DSC signal of powder and as-built Ti-6Al-4V during heating with 20 $\frac{K}{min}$ showing an exothermic and endothermic transition when deviating from the linear reference line (dashed-blue).

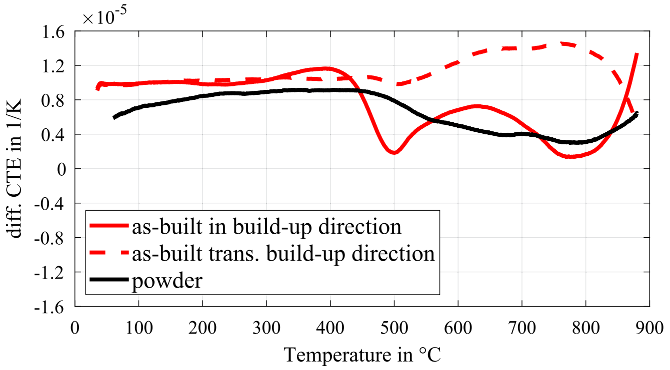

Fig. 5. Corresponding differential coefficient of linear thermal expansion over temperature of as-built in build-up direction, as-built transversal to build-up direction and powder sample.

441.7 °C and an extrapolated finish temperature θ_{ef1} of 604.9 °C. The associated transformation shows an exothermic heat effect with an absolute value of the transition enthalpy ΔH of 26.1 $\frac{J}{g}$ for powder and 15.2 $\frac{J}{g}$ for the as-built state. With ongoing heating, a second calorimetric event occurs starting at an extrapolated initial temperature θ_{ei2} of 835.8 °C (powder) and 826.5 °C (as-built) representing an endothermic transformation. This endothermic event could correspond to the β transformation. Compared to the literature on the β-transus of AM Ti-6Al-4V, this temperature appears relatively low. The DSC measurements alone do not allow for a definitive interpretation. In anticipation of the additional microstructural analyses and hardness measurements (see Fig. 6 (a)), it seems reasonable to assume that this combines β transformation and progressive grain coarsening. When comparing the data for as-built and powder samples, it is noticeable that the enthalpy values of the first peak are lower for the as-built samples, and the second peak is less pronounced. This could indicate the influence of the hierarchical martensitic structure in the as-built state. The fine and highly distorted structure may sterically hinder the transformations, potentially explaining the observed differences. Since the characteristics of the DSC signals depend on thermal inertia and are also influenced by heating rates, a conclusive answer must be provided outside the scope of this study.

In addition to calorimetric measurements, the trend of the differential coefficient of linear thermal expansion from TMA provides valuable insights regarding internal crystallographic and morphological changes. The differential coefficient of linear thermal expansion α corresponds to the first derivative of the curve of the thermal expansion with respect to temperature. It is determined with initial sample length L_0, the relative change of the sample length δL at a differential temperature step $\delta\theta$ as [35]

$$\alpha(\theta) = \frac{1}{L_0} \cdot \frac{\delta L}{\delta \theta}. \tag{3}$$

The results for the differential coefficient of linear thermal expansion (CTE) are shown in Fig. 5. Coupled with the investigated onset temperatures, a more complex behavior becomes evident, particularly along the build-up direction. In this direction, the thermal behavior is governed solely by the characteristic AM martensitic structure, uninfluenced by interruptions from former grain boundaries. This key aspect is the focus of the study, although valuable insights can also be gained by analyzing similarities in the microstructure. To fully leverage the potential of thermal analysis as a powerful investigative tool, it is crucial to correlate the observed results with the corresponding microstructural transition mechanisms.

Consequently, further material characterizations were conducted on heat-treated samples, with holding temperatures selected based on the observed CTE and DSC curves. The selected temperatures were 400 °C, 500 °C, 650 °C, 850 °C, and 1000 °C. Fig. 6 illustrates these results, including (a) Vickers hardness measurements, (b) an SEM micrograph of an as-built sample, and (c–g) micrographs of samples subjected to the respective holding temperatures.

The hardness indicates no significant difference between the as-built sample and those exposed to a temperature of 400 °C. However, beyond 400 °C, the hardness values increase significantly, rising from 366 HV5 to a maximum of 399 HV5 at 500 °C. Subsequently, the hardness values decline to a minimum of 355 HV5 at 850 °C before experiencing a slight increase up to 1000 °C. The SEM micrographs reveal the evolution of microstructure across the different temperature steps. Between the as-built and the 400 °C condition no visible differences are observed. At 500 °C, white specks emerge, representing nanosized β particles [36]. At further annealing to 650 °C, the microstructure evolves with the precipitation of the nano-particles into fine β films within the acicular structure. At 850 °C, significant coarsening of the microstructure occurs, characterized by a stabilized lamellar structure comprising α and β phases. Finally, at 1000 °C, the resultant structure is distinctly different, characterized by non-oriented needle-like features dominating the morphology alongside a stable $\alpha+\beta$ microstructure. It is reasonable to conclude that the observed martensite results from subsequent water quenching, while the PBF-LB/M-induced martensite is entirely transformed. Based on additional SEM images, an image particle analysis was performed to study transformation in the acicular size distribution. As the modifications are expected to begin in the fine fractions of the structure, the focus will be on the smaller fragments of the microstructure. Yang et al. classified these fragments as secondary martensite, characterized by the length of the martensite needles ranging from 1-2 µm [10]. In the image particle analysis, the needles were evaluated by the length of the major axis, the length of the minor axis, and the angle between the horizontal and the major axis (see illustration Fig. 7 (a). Fig. 7 (b-d) exemplarily displays the evaluation results for the as-built condition.

The DSC data, the observed propagation of the CTE, and the marked increase in Vickers hardness suggest that a microstructural transformation initiates at around 400 °C. However, SEM results did not provide significant insights.

Existing literature points to microstructural diffusion mechanisms within the sub-nanometer scale as a potential factor [36,37]. To further investigate this, a sample was subjected to annealing at 475 °C for 24 hours to provoke the underlying mechanisms. Together with an as-built sample XRD analysis was conducted to assess the quantitative variations in phase fractions through Rietveld refinement. Fig. 8 illustrates the XRD diffractograms, while Table 2 details the identified phase fractions. The potential phase fractions were established, with the hcp α phase designated as P63\mmc (#194, Mg type), and the bcc β phase identified as Im$\bar{3}$m (#229, W type). The disturbed martensitic α' cannot be differentiated from the α phase, as variations in lattice parameters and composition are considered to be minimal. The evaluation of the as-built condition shows that 100% of the morphology is in the martensitic phase, consistent with the SEM images' observations.

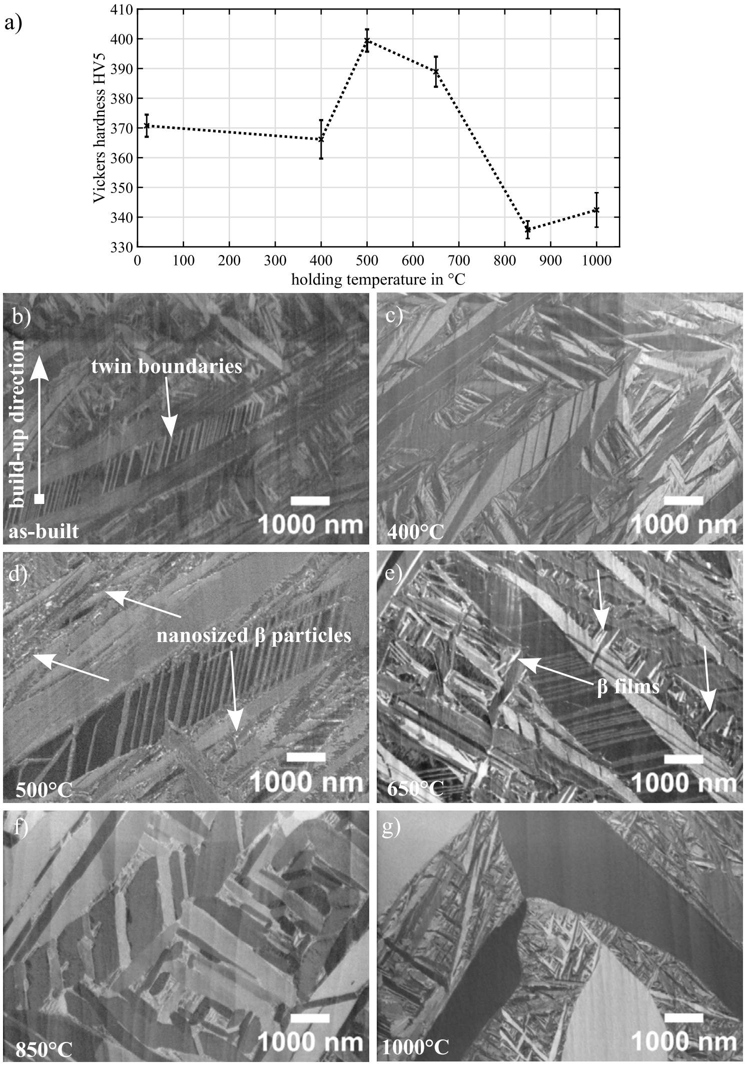

Fig. 6. Examination of the microstructure utilizing the hardness profile HV (a) and 25kX SEM images (build-up direction upwards) of as-built (b) and heat-treated samples at 400 °C (c), 500 °C (d), 650 °C (e), 850 °C (f), and 1000 °C (g) for 30 minutes and water quenching.

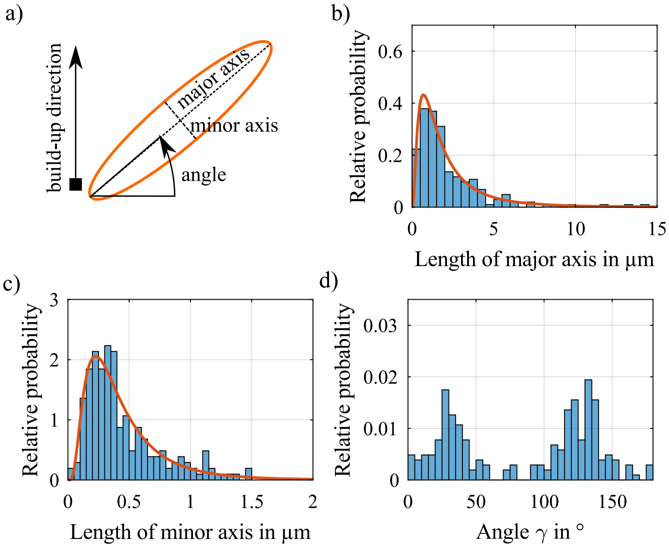

Fig. 7. Evaluation criteria for image particle analysis a) and the exemplarily distribution of the length of major axis (b), length of minor axis distribution (c) and angle alignment (d) of secondary martensite in as-built condition.

Table 2
Results of quantitative Rietveld phase analysis of as-built and 475 °C 24 hours annealed condition and goodness of fit (GOF).

Condition	α/α'	β	Ti_3Al	GOF
as-built	100%	0%	0%	1.68
475 °C	85%	5%	10%	1.83

In contrast, the heat-treated samples display additional reflections, indicating the presence of a β phase. Furthermore, as indicated by current literature [36,37], these peaks have been fitted with intermetallic Ti_3Al (P63\mmc), resulting in a satisfactory fit. The heat-treated samples exhibit a β phase content of 5%, suggesting that β precipitation begins at sub-nano dimensions, as no noticeable changes are detected in the SEM images of samples treated at 500 °C. The phase fraction analysis also indicates that the intermetallic phase constitutes 10% of the overall composition.

The findings provide critical insights into the transformations of PBF-LB/M Ti-6Al-4V during thermal exposure. In as-built conditions, the predominant microstructure is characterized by the martensitic α' phase, a direct consequence of the specific temperature history associated with the additive manufacturing process [10]. This fine, needle-like martensite exhibits a hierarchical size distribution and alignment (see Fig. 7)

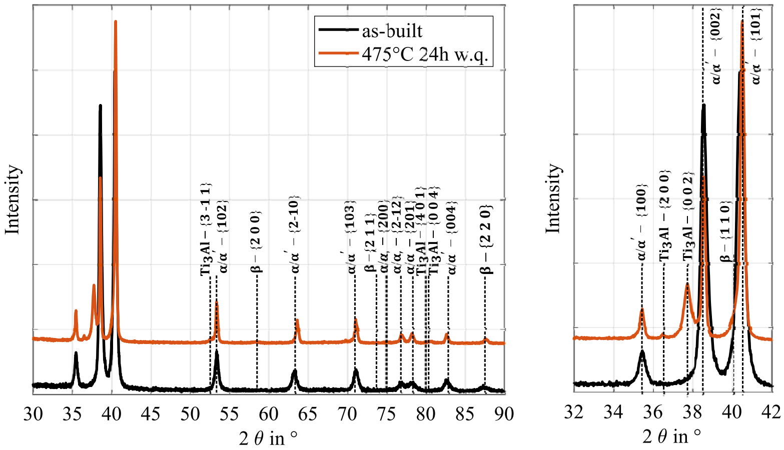

Fig. 8. 1D diffractograms comparing the as-built sample to one annealed at 475 °C highlighting the variations in phase fractions, evidenced by the emergence of additional β and Ti_3Al reflections.

between prior β grain boundaries and twin structures (see Fig. 6(b)), indicating the shear-dominated formation mechanism that leads to a microstructure significantly out of thermodynamic equilibrium. Up to a temperature of 400 °C, no significant changes were observed, and the elongation characteristics are determined by thermal expansion of α' phase [37]. A subsequent rise in temperature from 400 °C to 500 °C leads to a significant reduction in CTE. This behavior is driven by the start of sub-nano-scale β precipitation observed in phase analysis and the accompanied segregation by forcedly dissolved Vanadium. Haubrich et al. [36] observed the diffusion of Vanadium, which was highlighted by an increasing Vanadium concentration in β to a maximum as shown through HEXRD and atom-probe tomography within this temperature range [36]. The deliberate incitement of the mechanism in this study showed that this segregation through Vanadium diffusion provides the prerequisite for a sufficient formation of intermetallic Ti_3Al. This formation of the hard intermetallic Ti_3Al dominates over the precipitation of the softer nanosized β phase, which is related to the significant increases in hardness. This hardening occurs at PBF-LB/M process-relevant times and temperatures, such as within heat accumulations. In combination with the residual stresses created during the process, this embrittlement can result in crack formation or fracture, leading to irreversible damage within the component during the manufacturing process. In the current literature, first relaxation processes of residual stresses were also detected above 400 °C [37]. The changing trend of the CTE at 500 °C into an increase represents a variation in the microstructural transformation. This could be linked to the dissolving of the Vanadium enrichments in the β phase fraction [36]. The appearance of the nano-particles, as seen in the SEM images (see Fig. 6(c)) indicates the persistent growth and stabilization of β, which favor this mechanism. The stated insights suggest that as an effect, the concentrated Vanadium is distributed in the increasing β phase fraction, the intermetallic Ti_3Al decomposes. This finding is corroborated by the reported reduction from the hardness peak at 500 °C, further dominated by a softening trend-driven rise of β content. This process of crystal recovery through recrystallization, which entails the precipitation and decomposition of the intermetallic compound Ti_3Al due to diffusion of forcibly dissolved Vanadium, is thought to be responsible for the exothermic peak noted in the DSC analysis. This exothermic event was characterized by an initial temperature $\theta_{\mathrm{ei}1}$ of 441.7 °C and an efinal temperature $\theta_{\mathrm{ef}1}$ of 604.9 °C, which represents as completed mechanism to the specified temperatures. The evolution from 650 °C onwards is characterized by the ongoing stress relaxation and the starting transformation of $\alpha' \rightarrow \alpha + \beta$. This transformation becomes evident by the again reducing CTE and the coarsening of acicular to a more lamellar microstructure (see SEM image in Fig. 6(f)). The image particle analysis shown in Fig. 9 reveals that the coarsening at 850 °C is mainly distinct by the growth in length of the minor axis of the grains. As a consequence, the hardness drops further between 650 °C and 850 °C.

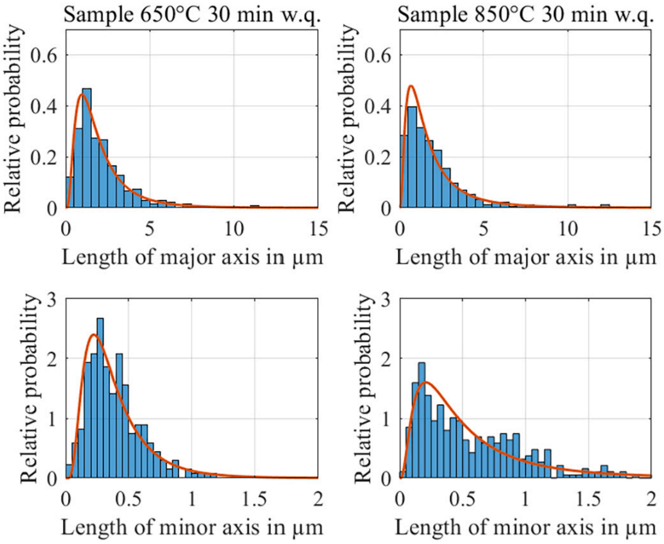

Fig. 9. Comparison of the needle major and minor axis distribution indicates the increase between the sample at 650 °C (left) and 850 °C (right), indicating the coarsening in the microstructure.

Finally, the rise in CTE and the endothermic effect (at onset 826.5 °C for as-built conditions) at the upper end of the investigated temperature range marks the decomposition of the structure followed by a slight incline in hardness with further heating. During this decomposition, all remaining α' and α phase fractions decay until exclusively β is present after heating beyond the β-transus temperature. Fig. 6(g) shows the corresponding microstructure with stable $\alpha + \beta$ morphology—the non-orientated, nano-sized α' martensite results from subsequent water-quenching of the samples. In this case, the volume fraction of the reformed martensite is still influenced by the heating temperature [38]. As the temperature rises, the martensite transformation process is promoted. As a result, the more significant volume fraction of the subsequent water-quenched martensitic microstructure and the finer martensitic structure are likely responsible for the hardness increase observed in the temperature range between 850 °C and 1000 °C. The CTE behavior of the sample tested transversal to the build direction shows similar trends but is less pronounced. The assumed recrystallization related to the intermetallic phase, followed by coarsening, is noticeably weaker. This can be attributed to the previous columnar structure of the former β grains and the alignment of the martensite. These persistent

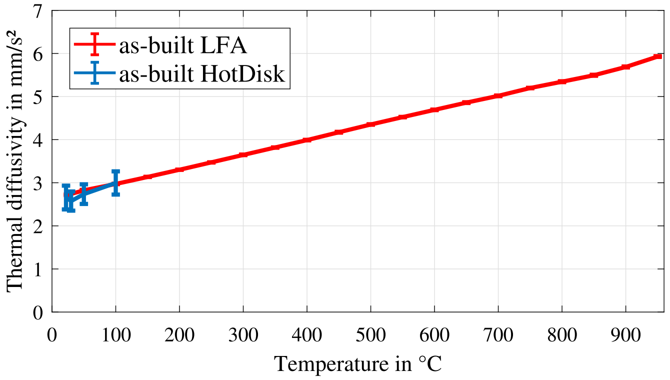

Fig. 10. Thermal diffusivity of as-built Ti-6Al-4V by LFA and hot disk method.

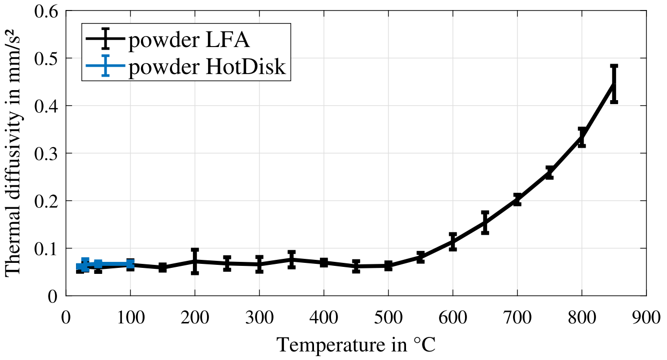

Fig. 11. Thermal diffusivity of powder sample by LFA and hot disk method.

boundaries reduce the effects of transformations. Notably, the transition to the β phase occurs simultaneously to the CTE trend of the as-built sample tested in the build-up direction. The CTE of the powder condition demonstrates the identified settling effects at lower temperatures. The trend indicates a change at approximately 500 °C, which may be associated with the reduction of residual stresses and the decomposition of martensite. Moreover, the exothermic event in the DSC could indicate the precipitation of β and the intermetallic Ti_3Al through the segregation of Vanadium. The fact that this aspect is less pronounced in the CTE trend of the powder could suggest a link between the martensitic size or directional dependence and the intermetallic phase formation. The effect on the change in length is less prominent maybe due to the random orientation of martisite within the particles (see micrograph in Fig. 1). The martensite was created during the rapid cooling process in powder production (gas atomization) and consequently did not exhibit the hierarchical PBF-LB/M morphology. The decomposition mechanism becomes notably pronounced when the material reaches temperatures beyond the β-transus, indicating a critical transition point where structural changes are initiated. This further underscores the exceptional nature of the AM-specific Ti-6Al-4V microstructure, making the knowledge of it essential for achieving excellence in quality assurance and process optimization.

3.3. Thermal diffusivity

In addition, to the microstructural features and transformations occurring in the global process temperature range, the present study aimed to evaluate the thermal diffusivity of AM Ti-6Al-4V. This was achieved by utilizing the LFA and HotDisk® methods. The experimental LFA data for as-built Ti-6Al-4V was analyzed using the standard model of the provided preprocessing software according to Cape et al. [39]. The theory of this model considers two-dimensional heat flux, multi-surface heat loss, and radiation and is intended for solid samples. Fig. 10 shows the results for thermal diffusivity of the as-built samples derived from both the LFA and HotDisk® method. The thermal diffusivity of LFA measurement shows a linear trend over the temperature range up to 950 °C. The data measured by LFA and HotDisk® in the lower temperature region provide reasonable values expected for PBF-LB/M processed Ti-6Al-4V [23]. The minor standard deviation of LFA data can be attributed to the shielded setup and the automated procedure providing more stable conditions during analysis.

In the LFA evaluation of the powder samples, the best-fit results are achieved with the implemented penetration model (according to MacMasters et al. [40]), which considers one-dimensional heat flux, surface heat loss, porosity, and inhomogeneous energy absorption at the sample surface. The thermal diffusivity results are shown in Fig. 11. Up to 100 °C, both transient analysis methods lead to comparable results and thus validate each other.

As the temperature increases, the LFA results exhibit a nonmonotonic trend until the values rise significantly above 500 °C. This behavior was also investigated in recent studies on AM Ti-6Al-4V powders [29,24] and referred to the driving heat transfer mechanism, which is temperature-dependent. Under PBF-LB/M process conditions (argon gas and pressure), the heat transfer in lower temperatures is primarily determined by conduction through the process gas as heat transfer between particles is limited by the temperature-independent contact resistance at particle-to-particle interfaces [28,24]. As the temperature increases, the powder particles start sintering and forming agglomerates. Therefore, the contact areas are increasing, which promotes heat conduction. Furthermore, the effect of radiation is enhanced exponentially [28]. Consequently, the start of powder sintering is associated with the 500 °C onset temperature. A similar effect can be observed in the fit results of the individual IR-detector signals of the LFA. In the nonmonotonic trend range, the data fitting with the penetration model delivers sufficient quality parameters with randomly distributed residues. In the range of increasing diffusivity values, the fit quality shows deficiencies, illustrated by the IR-detector signal and penetration model fit of shot 53 at 500 °C compared to shot 65 at 700 °C in Fig. 12. This circumstance can be linked to the change in the primary heat transfer mechanism, which is not accounted by the assumptions of available LFA evaluation models. Developing an appropriate evaluation model for powder analysis remains an area for further research. Nevertheless, the results indicate that both transient methods are capable of powder evaluation. Even LFA is more straightforwardly applied for higher temperatures and is more likely to evaluate AM powders as smaller sample masses are required.

3.4. Specific heat capacity and effective thermal conductivity

The isobaric specific heat capacity is a property that describes the energy required to raise the temperature of a given amount of substance by 1 Kelvin while keeping the pressure constant. This property is applicable only if the material does not undergo any first-order phase transformations. As reported in Chapter 2.3, the specific heat capacities of an as-built and powder sample were analyzed considering baseline, sapphire standard, and sample measuring runs in DSC. Based on these measurements, the specific heat capacity of the sample $c_{\mathrm{p,sample}}$ can be calculated with:

$$c_{\mathrm{p,sample}}(\theta) = \frac{m_{\mathrm{standard}}}{m_{\mathrm{sample}}} \cdot \frac{(u_{\mathrm{sample}}(\theta) - u_{\mathrm{baseline}}(\theta))}{(u_{\mathrm{standard}}(\theta) - u_{\mathrm{baseline}}(\theta))} \cdot c_{\mathrm{p,standard}}(\theta), \qquad (4)$$

where m_{standard} is the mass of the sapphire standard, m_{sample} is the sample mass, u_{sample} is the DSC signal of the sample run, u_{baseline} is the signal of the baseline run, u_{standard} is the DSC signal of the sapphire standard, and $c_{\mathrm{p,standard}}$ is the specific heat capacity of the sapphire standard. Under a continuum mechanical approach, a powder's thermal properties are considered as lumped and described with effective material parameters. The effective specific heat capacity of a finite powder volume $c_{\mathrm{p,eff}}$ is determined in approximation with the mass fractions of the process gas $\frac{m_{\mathrm{gas}}}{m_{\mathrm{total}}}$, the specific heat capacity of the process gas $c_{\mathrm{p,gas}}$, the mass

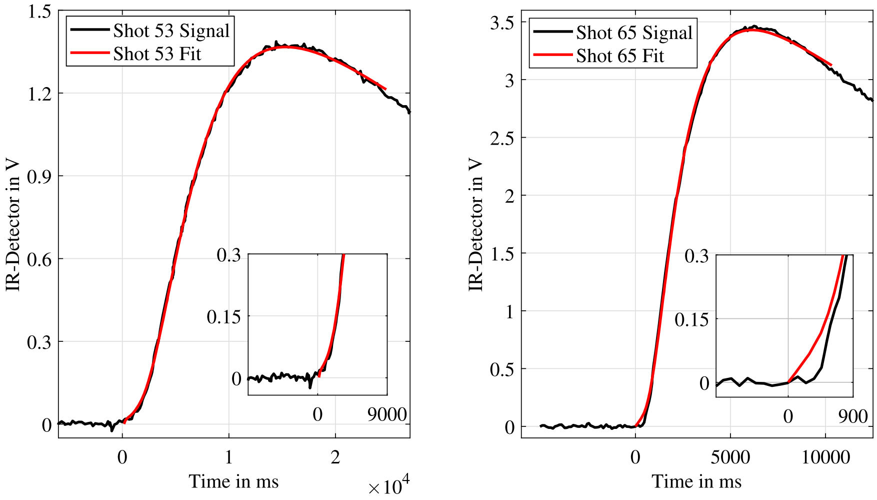

Fig. 12. Raw IR-Detector signal of LFA measurement with penetration model fit of shot 53 at 500 °C (left) and shot 65 at 700 °C (right) of powder sample.

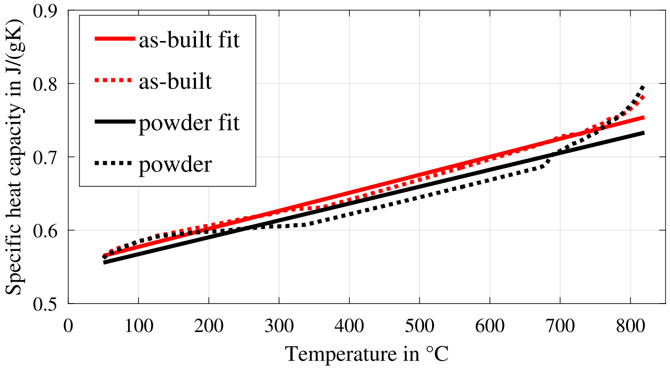

Fig. 13. Specific heat capacity of as-built and powder sample.

fraction of the particle material $\frac{m_{solid}}{m_{total}}$, and the specific heat capacity of the particle material $c_{p,solid}$ [41]:

$$c_{p,eff} = \frac{m_{gas}}{m_{total}} \cdot c_{p,gas} + \frac{m_{solid}}{m_{total}} \cdot c_{p,solid} \approx c_{p,solid}; \tag{5}$$

Taking further into account that the mass fraction of the process gas in the finite volume is low, the assumption applies that the effective heat capacity of the powder is primarily determined by the specific heat capacity of the particle material (compare the density of argon with 1.6 $\frac{kg}{m^3}$ [42] and solid Ti-6Al-4V with 4430 $\frac{kg}{m^3}$ [43,44] at room temperature [41,45,42]). Fig. 13 shows the results of the as-built and powder samples with extrapolation over the exothermic peak range, including a linear fit. The slightly lower values of the powder could be attributed to the contact resistance of heat transfer of the powder particle and the DSC crucible.

In general, from the fundamental heat transfer equation, the thermal conductivity is determined by:

$$\lambda(\theta) = a(\theta) \cdot c_p(\theta) \cdot \rho(\theta), \tag{6}$$

with the thermal diffusivity a, the specific heat capacity c_p, and the density ρ. Fig. 14 represents the results derived from the temperature-dependent experimental data compared to literature values of conventional $\alpha+\beta$ Ti-6Al-4V [43]. It can be concluded that thermal properties comparable to conventional solid Ti-6Al-4V can be achieved with suitable process parameters.

Given the lack of data on the effective thermal conductivity λ_{eff} of PBF-LB metal powders, these are calculated in simulations from the solid-state thermal conductivity λ_{solid} in connection with the porosity of the powder bed Φ by:

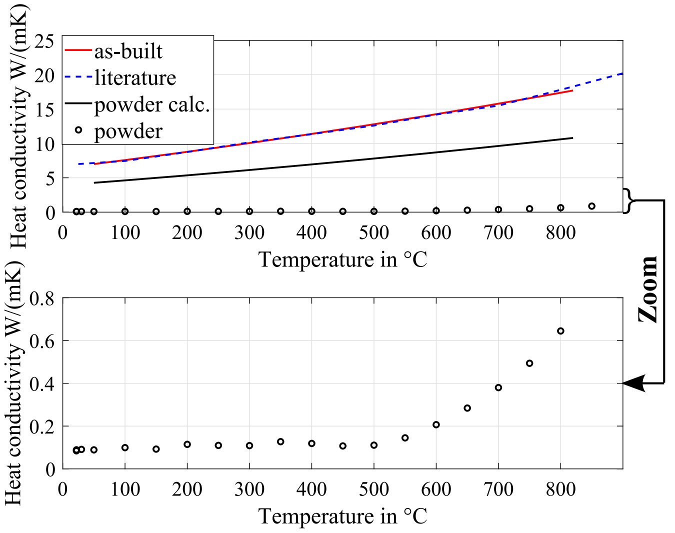

Fig. 14. Thermal conduction of as-built compared to literature values of solid Ti-6Al-4V and effective thermal conductivity of powder.

$$\lambda_{eff}(\theta) = (1 - \Phi) \cdot \lambda_{solid}(\theta). \tag{7}$$

Based on the apparent density of the powder samples (see Chapter 2.5) and the density of solid Ti-6Al4-V from literature [43], the powder bed porosity is found to be 0.39. Therefore, the effective thermal conductivity is determined using the results of the as-built samples and equation (7) (see Fig. 14). By comparing the result calculated and the experimentally obtained data, it can be observed that the equation overestimates the effective thermal conductivity of AM powders and does not consider sintering processes and the associated change in heat transfer behavior. Lui et al. [24] showed that the prediction of analytical models based on temperature-dependent properties of the solid material and gas properties is not feasible to predict the effective thermal conductivity of AM powders reliably. Therefore, such assumptions are unsuitable for predicting the heat transfer from the solid to the powder and thus cannot be used to predict heat build-up in the AM process.

4. Conclusion

Understanding the thermophysical properties across the global temperature field is crucial, as these properties significantly influence heat flow during the PBF-LB/M process. This study provides a comprehensive experimental characterization of Ti-6Al-4V in its processed state via laser powder bed fusion (PBF-LB/M) and its powder state, employing thermal analysis techniques. Characterization of the microstructure allowed meaningful insights into the effect of microstructural transformation on temperature-dependent macroscopic behavior, enhancing the interpretation and discussion of derived data. The microstructural transformation of PBF-LB/M processed Ti-6Al-4V under heating was described using calorimetry, the trend of the coefficient of thermal expansion, Vickers hardness testing, SEM, and XRD.

Up to 400 °C, thermal elongation is primarily influenced by the expansion of crystals within the fully martensitic microstructure. It is presumed that the initial precipitation and the diffusion of forcibly dissolved Vanadium are sufficient to promote the formation of intermetallic Ti_3Al phase, significantly increasing Vickers hardness. The intermetallic phase begins to decompose when temperatures exceed approximately 500 °C. The recrystallization and crystal recovery, including the precipitation and decomposition of the Ti_3Al intermetallic phase, results in an exothermic peak observed in calorimetry, accompanied by a reversal in the trend of thermal expansion. As a driving effect, the precipitation of the β phase is suspected. Beyond around 650 °C, both coarsening and the growth and stabilization of the β phase lead to further reductions in thermal expansion and hardness. The complete transformation of the microstructure to the pure β phase is characterized by an endothermic peak. In the transverse direction to the build-up orientation, thermal elongation behavior is influenced by prior β grain boundaries, leading to a diminished impact from microstructural transformations. The findings, characterized by the hardness trend, reveal the complexity of the material's behavior in inhomogeneous heat removal during PBF-LB/M. Differences in hardness indicate embrittlement favoring potential crack initiation, leading to irreversible failure of component quality. From this, heat accumulation in this temperature range should be avoided, although the actual influence on components is the object of future research.

Settling effects, crystal elongation, and the relaxation of residual stresses influence the thermal expansion characteristic of the AM powder state. Sintering of powder particles affects the thermal diffusivity measured with the laser flash method, which indicates a significant change in the heat transfer mechanism within the powder. Notably, the transient plane source method validated laser flash measurements. Beyond the benefits and limitations of experimental analysis methods utilizing AM powders, this research offers comprehensive data on thermophysical properties that contribute to the advancement of the field.

The evaluation of heat conductivity based on the experimental data reveals that the simplified assumptions often employed for temperature-dependent thermal conductivity of AM powders in simulations may not adequately capture the complexities of the material behavior. This research provides a detailed database of thermophysical properties. It paves the way for thermophysical material modeling, enabling precise future investigations of process heat flow with detailed process planning and optimization.

CRediT authorship contribution statement

J. Rottler: Writing – review & editing, Writing – original draft, Visualization, Methodology, Investigation. **T.K. Tetzlaff:** Writing – review & editing, Methodology, Investigation. **A. Wohninsland:** Writing – review & editing, Investigation. **A. Lion:** Writing – review & editing, Supervision, Project administration, Funding acquisition. **M. Johlitz:** Writing – review & editing, Supervision, Project administration, Funding acquisition.

Declaration of competing interest

The authors declare that they have no known competing financial interests or personal relationships that could have appeared to influence the work reported in this paper.

Acknowledgement

This research [project FLAB-3Dprint] is funded by dtec.bw – Digitalization and Technology Research Center of the Bundeswehr in cooperation with the Bundeswehr Research Institute for Materials, Fuels and Lubricants (WIWeB) which we gratefully acknowledge. dtec.bw is funded by the European Union – NextGenerationEU. The WIWeB is under the responsibility of the German Federal Ministry of Defense.

Data availability

Data will be made available on request.

References

[1] K. Cooper, P. Steele, B. Cheng, K. Chou, Contact-free support structures for part overhangs in powder-bed metal additive manufacturing, Inventions 3 (1) (2018) 2, https://doi.org/10.3390/inventions3010002.

[2] K. Zhang, G. Fu, P. Zhang, Z. Ma, Z. Mao, D.Z. Zhang, Study on the geometric design of supports for overhanging structures fabricated by selective laser melting, Materials 12 (1) (2018), https://doi.org/10.3390/ma12010027.

[3] S. Liu, Y.C. Shin, Additive manufacturing of Ti6Al4V alloy: a review, Mater. Des. 164 (2019) 107552, https://doi.org/10.1016/j.matdes.2018.107552.

[4] F. Calignano, Design optimization of supports for overhanging structures in aluminum and titanium alloys by selective laser melting, Mater. Des. 64 (2014) 203–213, https://doi.org/10.1016/j.matdes.2014.07.043.

[5] J. Grünewald, P. Clarkson, R. Salveson, G. Fey, K. Wudy, Influence of pulsed exposure strategies on overhang structures in powder bed fusion of Ti6Al4V using laser beam, Metals 11 (7) (2021) 1125, https://doi.org/10.3390/met11071125.

[6] Z. Wu, S.P. Narra, A. Rollett, Exploring the fabrication limits of thin-wall structures in a laser powder bed fusion process, Int. J. Adv. Manuf. Technol. 110 (1–2) (2020) 191–207, https://doi.org/10.1007/s00170-020-05827-4.

[7] S. Clijsters, T. Craeghs, J.-P. Kruth (Eds.), A Priori Process Parameter Adjustment for SLM Process Optimization, Taylor & Francis Group, 2012.

[8] P.A. Hooper, Melt pool temperature and cooling rates in laser powder bed fusion, Addit. Manuf. 22 (2018) 548–559, https://doi.org/10.1016/j.addma.2018.05.032.

[9] J.J.S. Dilip, S. Zhang, C. Teng, K. Zeng, C. Robinson, D. Pal, B. Stucker, Influence of processing parameters on the evolution of melt pool, porosity, and microstructures in Ti-6Al-4V alloy parts fabricated by selective laser melting, Prog. Addit. Manuf. 2 (3) (2017) 157–167, https://doi.org/10.1007/s40964-017-0030-2.

[10] J. Yang, H. Yu, J. Yin, M. Gao, Z. Wang, X. Zeng, Formation and control of martensite in Ti-6Al-4V alloy produced by selective laser melting, Mater. Des. 108 (2016) 308–318, https://doi.org/10.1016/j.matdes.2016.06.117.

[11] M. Liu, L.N. Chiu, D. Liu, A. Huang, C. Davies, X. Wu, W. Yan, A macroscale thermal simulation strategy with track-scale resolution for laser powder bed fusion, Mater. Des. 226 (2023) 111622, https://doi.org/10.1016/j.matdes.2023.111622.

[12] M. Chen, M. Simonelli, S. van Petegem, Y. Yau Tse, C. Sin Ting Chang, M. Grazyna Makowska, D. Ferreira Sanchez, H. Moens-Van Swygenhoven, A quantitative study of thermal cycling along the build direction of ti-6al-4v produced by laser powder bed fusion, Mater. Des. 225 (2023) 111458, https://doi.org/10.1016/j.matdes.2022.111458.

[13] T. Ahmed, H.J. Rack, Phase transformations during cooling in $\alpha+\beta$ titanium alloys, Mater. Sci. Eng. A 243 (1–2) (1998) 206–211, https://doi.org/10.1016/S0921-5093(97)00802-2.

[14] L. Thijs, F. Verhaeghe, T. Craeghs, J. van Humbeeck, J.-P. Kruth, A study of the microstructural evolution during selective laser melting of Ti-6Al-4V, Acta Mater. 58 (9) (2010) 3303–3312, https://doi.org/10.1016/j.actamat.2010.02.004.

[15] Z. Liang, Z. Sun, W. Zhang, S. Wu, H. Chang, The effect of heat treatment on microstructure evolution and tensile properties of selective laser melted Ti6Al4V alloy, J. Alloys Compd. 782 (2019) 1041–1048, https://doi.org/10.1016/j.jallcom.2018.12.051.

[16] R. Dabrowski, The kinetics of phase transformations during continuous cooling of the Ti6Al4V alloy from the single-phase beta range, Arch. Metall. Mater. 56 (3) (2011) 703–707, https://doi.org/10.2478/v10172-011-0077-x.

[17] A.M. Beese, B.E. Carroll, Review of mechanical properties of ti-6Al-4V made by laser-based additive manufacturing using powder feedstock, JOM 68 (3) (2016) 724–734, https://doi.org/10.1007/s11837-015-1759-z.

[18] L. Novotny, M. Berevs, H.F.G. de Abreu, J. Zajac, W. Bleck, Thermal analysis and phase transformation behaviour during additive manufacturing of Ti-6Al-4V alloy, Mater. Sci. Technol. 35 (7) (2019) 846–855, https://doi.org/10.1080/02670836.2019.1593669.

[19] X.P. Ren, H.Q. Li, H. Guo, F.L. Shen, C.X. Qin, E.T. Zhao, X.Y. Fang, A comparative study on mechanical properties of Ti-6Al-4V alloy processed by additive manufacturing vs. traditional processing, Mater. Sci. Eng. A 817 (2021) 141384, https://doi.org/10.1016/j.msea.2021.141384.

[20] M.A. Buhairi, F.M. Foudzi, F.I. Jamhari, A.B. Sulong, N.A.M. Radzuan, N. Muhamad, I.F. Mohamed, A.H. Azman, W.S.W. Harun, M.S.H. Al-Furjan, Review on volumetric

energy density: influence on morphology and mechanical properties of Ti6Al4V manufactured via laser powder bed fusion, Prog. Addit. Manuf. 8 (2) (2023) 265–283, https://doi.org/10.1007/s40964-022-00328-0.

[21] P. Metalnikov, G. Ben-Hamu, D. Eliezer, Corrosion behavior of AM-Ti-6Al-4V: a comparison between EBM and SLM, Prog. Addit. Manuf. 7 (3) (2022) 509–520, https://doi.org/10.1007/s40964-022-00293-8.

[22] J. Liu, G. Li, Q. Sun, H. Li, J. Sun, X. Wang, Understanding the effect of scanning strategies on the microstructure and crystallographic texture of Ti-6Al-4V alloy manufactured by laser powder bed fusion, J. Mater. Process. Technol. 299 (2022) 117366, https://doi.org/10.1016/j.jmatprotec.2021.117366.

[23] K. Bartsch, D. Herzog, B. Bossen, C. Emmelmann, Material modeling of Ti-6Al-4V alloy processed by laser powder bed fusion for application in macro-scale process simulation, Mater. Sci. Eng. A 814 (2021) 141237, https://doi.org/10.1016/j.msea.2021.141237.

[24] M. Liu, L.N. Chiu, H. Shen, X. Fang, Z. Tao, A. Huang, C. Davies, X. Wu, W. Yan, Effective thermal conductivities of metal powders for additive manufacturing, Powder Technol. 401 (2022) 117323, https://doi.org/10.1016/j.powtec.2022.117323.

[25] S. Zhang, B. Lane, J. Whiting, K. Chou, On thermal properties of metallic powder in laser powder bed fusion additive manufacturing, J. Manuf. Process. 47 (2019) 382–392, https://doi.org/10.1016/j.jmapro.2019.09.012.

[26] M. de Beer, P.G. Rousseau, C.G. Du Toit, A review of methods to predict the effective thermal conductivity of packed pebble beds, with emphasis on the near-wall region, Nucl. Eng. Des. 331 (2018) 248–262, https://doi.org/10.1016/j.nucengdes.2018.02.029.

[27] W. van Antwerpen, C.G. Du Toit, P.G. Rousseau, A review of correlations to model the packing structure and effective thermal conductivity in packed beds of mono-sized spherical particles, Nucl. Eng. Des. 240 (7) (2010) 1803–1818, https://doi.org/10.1016/j.nucengdes.2010.03.009.

[28] L.C. Wei, L.E. Ehrlich, M.J. Powell-Palm, C. Montgomery, J. Beuth, J.A. Malen, Thermal conductivity of metal powders for powder bed additive manufacturing, Addit. Manuf. 21 (2018) 201–208, https://doi.org/10.1016/j.addma.2018.02.002.

[29] F. Ahsan, J. Razmi, L. Ladani, Experimental measurement of thermal diffusivity, conductivity and specific heat capacity of metallic powders at room and high temperatures, Powder Technol. 374 (2020) 648–657, https://doi.org/10.1016/j.powtec.2020.07.043.

[30] ISO 13322-2, Particle size analysis-Image analysis methods - Part 2, Dynamic image analysis methods, 2021.

[31] DIN ISO 9276-6, Representation of results of particle size analysis - Part 6: Descriptive and quantitative representation of particle shape and morphology, 2012.

[32] EOS GmbH, Electro Optical Systems, Material data sheet: EOS Titanium Ti64ELI, 2022.

[33] H. Jia, H. Sun, H. Wang, Y. Wu, H. Wang, Scanning strategy in selective laser melting (SLM): a review, Int. J. Adv. Manuf. Technol. 113 (9–10) (2021) 2413–2435, https://doi.org/10.1007/s00170-021-06810-3.

[34] J.-C. Tseng, W.-C. Huang, W. Chang, A. Jeromin, T.F. Keller, J. Shen, A.C. Chuang, C.-C. Wang, B.-H. Lin, L. Amalia, N.-T. Tsou, S.-J. Shih, E.-W. Huang, Deformations of Ti-6Al-4V additive-manufacturing-induced isotropic and anisotropic columnar structures: insitu measurements and underlying mechanisms, Addit. Manuf. 35 (2020) 101322, https://doi.org/10.1016/j.addma.2020.101322.

[35] S. Vyazovkin, N. Koga, C. Schick, Handbook of Thermal Analysis and Calorimetry: Recent Advances, Techniques and Applications, 2 ed., Elsevier, 2018.

[36] J. Haubrich, J. Gussone, P. Barriobero-Vila, P. Kürnsteiner, E.A. Jägle, D. Raabe, N. Schell, G. Requena, The role of lattice defects, element partitioning and intrinsic heat effects on the microstructure in selective laser melted Ti-6Al-4V, Acta Mater. 167 (2019) 136–148, https://doi.org/10.1016/j.actamat.2019.01.039.

[37] P.P. Dhekne, M. Bönisch, M. Seefeldt, K. Vanmeensel, In-situ synchrotron X-ray diffraction investigation of martensite decomposition in laser powder bed fusion (L-PBF) processed Ti-6Al-4V, Mater. Sci. Eng. A 899 (2024) 146421, https://doi.org/10.1016/j.msea.2024.146421.

[38] S.Q. Wu, Y.J. Lu, Y.L. Gan, T.T. Huang, C.Q. Zhao, J.J. Lin, S. Guo, J.X. Lin, Microstructural evolution and microhardness of a selective-laser-melted Ti-6Al-4V alloy after post heat treatments, J. Alloys Compd. 672 (2016) 643–652, https://doi.org/10.1016/j.jallcom.2016.02.183.

[39] J.A. Cape, G.W. Lehman, Temperature and finite pulse-time effects in the flash method for measuring thermal diffusivity, J. Appl. Phys. 34 (7) (1963) 1909–1913, https://doi.org/10.1063/1.1729711.

[40] R.L. McMasters, J.V. Beck, R.B. Dinwiddie, H. Wang, Accounting for penetration of laser heating in flash thermal diffusivity experiments, J. Heat Transf. 121 (1) (1999) 15–21, https://doi.org/10.1115/1.2825929.

[41] C.A. Wagner, Untersuchungen zum Selektiven Lasersintern von Metallen, 1st edition, Berichte aus der Produktionstechnik, vol. 2003/11, Shaker, Aachen, 2003.

[42] V. Seyda, Werkstoff- und Prozessverhalten von Metallpulvern in der laseradditiven Fertigung, Springer Berlin Heidelberg, Berlin, Heidelberg, 2018.

[43] K.C. Mills, Recommended Values of Thermophysical Properties for Selected Commercial Alloys, Woodhead, Cambridge, 2002.

[44] M. Tang, P.C. Pistorius, J.L. Beuth, Prediction of lack-of-fusion porosity for powder bed fusion, Addit. Manuf. 14 (2017) 39–48, https://doi.org/10.1016/j.addma.2016.12.001.

[45] J.W. Barlow, The measurement of the thermal properties and absorptances of powders near their melting temperatures, https://doi.org/10.15781/T2JS9HR3W, 2018.